Open access • Journal Article • DOI:10.1021/ACS.JCTC.9B01240

Reconciling Simulated Ensembles of Apomyoglobin with Experimental Hydrogen/Deuterium Exchange Data Using Bayesian Inference and Multiensemble Markov State Models. — Source link

Hongbin Wan, Yunhui Ge, Asghar M. Razavi, Vincent A. Voelz

Institutions: Temple University

Published on: 23 Jan 2020 - Journal of Chemical Theory and Computation (American Chemical Society)

Reconciling simulated ensembles of apomyoglobin with experimental HDX data using Bayesian inference and multi-ensemble Markov State Models

Hongbin Wan,[†] Yunhui Ge,[†] Asghar Razavi,[†,‡] and Vincent A. Voelz[*,†]

[†]*Department of Chemistry, Temple University, Philadelphia,PA 19122, USA*

[‡]*Current address: Weill Cornell Medicine 1300 York Ave, New York, NY, 10065, USA*

E-mail: voelz@temple.edu

Abstract

Hydrogen/deuterium exchange (HDX) is a powerful technique to investigate protein conformational dynamics at amino acid resolution. Because HDX provides a measurement of solvent exposure of backbone hydrogens, ensemble-averaged over potentially slow kinetic processes, it has been challenging to use HDX protection factors to refine structural ensembles obtained from molecular dynamics simulations. This entails two dual challenges: (1) identifying structural observables that best correlate with backbone amide protection from exchange, and (2) restraining these observables in molecular simulations to model ensembles consistent with experimental measurements. Here, we make significant progress on both fronts. First, we describe an improved predictor of HDX protection factors from structural observables in simulated ensembles, parameterized from ultra-long molecular dynamics simulation trajectory data, with a Bayesian inference approach used to retain the full posterior distribution of model parameters.

We next present a new method for obtaining simulated ensembles in agreement with experimental HDX protection factors, in which molecular simulations are performed at various temperatures and restraint biases, and used to construct multi-ensemble Markov State Models (MSMs). Finally, the BICePs algorithm (Bayesian Inference of Conformational Populations) is then used with our HDX protection factor predictor to infer which thermodynamic ensemble agrees best with experiment, and estimate populations of each conformational state in the MSM. To illustrate the approach, we use a combination of HDX protection factor restraints and chemical shift restraints to model the conformational ensemble of apomyoglobin at pH 6. The resulting ensemble agrees well with experiment, and gives insight into the all-atom structure of disordered helices F and H in the absence of heme.

Introduction

Hydrogen/deuterium exchange (HDX) is a powerful technique to investigate protein conformational dynamics at amino acid resolution.[1–6] In this technique, competition between the rates of exchange and the rates at which proteins exposing backbone amides can be used to probe a wide range of time scales, including very slow local and/or global unfolding/refolding dynamics. Exposed (unprotected) backbone amide hydrogens exchange with deuterated solvent according to the following kinetic model:

$$(\text{N-H})_c \underset{k_c}{\overset{k_o}{\rightleftharpoons}} (\text{N-H})_o \xrightarrow{k_{\text{int}}} (\text{N-D})_o \tag{1}$$

where k_o is the opening rate, k_c is the closing rate and k_{int} is the intrinsic exchange rate. The observed exchange rate, $k_{\text{ex}} = k_o k_{\text{int}}/(k_o + k_c + k_{\text{int}})$, is very sensitive to temperature, pH, and the neighbor-dependent folded-state stability of each amino acid.[7]

In the so-called EX1 regime, which occurs at high pH, high temperature or low stability, $k_c << k_{\text{int}}$, resulting in an exchange rate of $k_{\text{ex}} = k_o k_{\text{int}}/(k_o + k_{\text{int}})$. In the so-called EX2 regime, $k_c >> k_{\text{int}}$, i.e. the rate at which backbone amide hydrogens exchange with deuterium is slow compared to the rates at which backbone residues convert between "closed" conformations protected from exchange, and "open" conformations where exchange can occur. Therefore, the observed hydrogen/deuterium (HD) exchange rate, $k_{\text{ex}} = k_o k_{\text{int}}/(k_c + k_{\text{int}})$, can be used to measure the relative populations of the "open" and "closed" states, by comparing it to the intrinsic exchange rate, k_{int}, observed for an unstructured peptide. In this regime, the extent of protection for a residue i is characterized by a *protection factor*, $\text{PF}_i = k_{\text{int}}^{(i)}/k_{\text{ex}}^{(i)}$, which can be related to the apparent free energy difference between open and closed states, ΔG, through $\ln \text{PF}_i = \beta \Delta G_i$, where $\beta = 1/kT$.

Existing methods for modeling HDX protection factors

Because HDX protection factors reflect potentially fleeting excursions to solvent-exposed states ("open" states), it has been challenging to make direct connections between molecular simulations of native-state protein dynamics and HDX protection factors, both in (1) predicting HDX protection factors directly from simulated trajectory data, and in (2) using experimental protection factors as restraints in simulated ensembles. Below, we review some of the methodology that has been used previously.

Predicting HDX protection factors from trajectory data

Because most molecular simulations are unable to sample rare fluctuations on long time scales, much of the past work on predicting protection factors from trajectory data has relied on the correlation between structural observables and rare fluctuations, using proxy quantities such as solvent exposure and protein/solvent hydrogen bonding. Petruk et al. predicted protection from all-atom MD simulations of MAPK ERK2 protein using average solvent-accessible surface area and numbers of solvation waters for each backbone amide hydrogen as proxy structural variables.[8] Ma et al. have identified aggregation states of polymorphic amyloid β42 peptide through a combination of NMR HDX data and predicted protection factors using the ratio of the average number of hydrogen-bonds between amide hydrogens and water oxygens, and between amide hydrogens and carbonyl oxygens.[9] Sljoka et al. use average hydrogen bond strengths to quantify protein rigidity/flexibility, which they use with solvent accessibility of backbone amide hydrogens to predict HDX data of Sso AcP from NMR ensembles.[10] Kieseritzky et al. predict protection factors from MD simulations using hydrogen-bond occupancy, survival times, and fluctuations of backbone atoms and hydrogen bond length.[11] Resing et al. showed that a linear combination of surface distance, inverse number of hydrogen-bonds, and the shortest distance to the first turn of the helix could predict the protection factors of ERK2 kinase helices with a linear correlation coefficient of 0.78.[12]

In a similar strategy, first employed by Vendruscolo et al.,[13] experimental protection factors are modeled according to $\ln \mathrm{PF}_i = \beta_c \langle N_c \rangle_i + \beta_h \langle N_h \rangle_i$, where $\langle N_c \rangle_i$ is the average number of heavy-atom contacts with residue i and $\langle N_h \rangle_i$ is the average number of backbone hydrogen bonds. The parameters β_c and β_h can be determined by fitting the results of native-state protein simulations to experimental data.[13,14] An advantage of this model is the computation of structural observables solely through pairwise distances, which are easily amenable to restraints. Another benefit of this model is its physical interpretation; the terms $\beta_c \langle N_c \rangle_i$ and $\beta_h \langle N_h \rangle_i$ represent free energies of residue burial and hydrogen bonding, respectively.

Now that millisecond-long explicit-solvent MD trajectories have become available,[15,16] it has become possible to predict protection factors using a more mechanistic approach. Persson and Halle,[17] based on an analysis of the millisecond simulation trajectory of bovine pancreatic trypsin inhibitor (BPTI), have proposed that exchange-competent ("open") conformations can be modeled as having two water oxygens found simultaneously within 2.6$\AA$ of the amide hydrogen. Persuasively, they show that direct counts of the number of trajectory snapshots containing open versus closed states gives computed protection factors in very good agreement with experiment. Limiting the practicality of the approach are (1) the need to obtain ultra-long simulation trajectories including sampled water configurations, and (2) the fact that highly protected amide hydrogens are likely coupled to global unfolding events which are not necessarily sampled in millisecond trajectories (indeed, such highly protected hydrogen exchange rates are not considered in the Persson and Halles analysis). It is problematic to use this “two-water” criterion to restrain simulated ensembles, as it would require three-body terms impractical for most molecular simulations. Nevertheless, the success of this approach suggests that millisecond simulations should provide more information for parameterizing empirical models than previously possible.

Using experimental protection factors as restraints in simulated ensembles

Here, too, the inability of most simulations to sample fluctuations on long timescales makes it difficult to restrain ensemble-averaged structural observables correlated with backbone amide protection. One approach has been to use simple structural models enabling the enumeration of a complete statistical thermodynamic ensemble. In the DXCOREX method of Liu et al,[18] the statistical thermodynamic ensemble of the protein is modeled as a set of folding units (microstates) that are either folded or unfolded, allowing complete enumeration of the complete state space and state probabilities according to an empirical Gibbs free energy function that depends on the accessible surface area of polar and nonpolar microstates. The per-residue protection factors can then be calculated from the Boltzmann probabilities of folded vs. unfolded states.

Another approach is to use restraint-biased all-atom simulations to model structural ensembles. Typically, these methods are used to achieve partial or global unfolding of a protein to produce ensembles more consistent with experimental protection factors. To restrain ensemble-average quantities in all-atom molecular dynamics ensembles, Vendruscolo et al.[13] developed a method whereby multiple simulation replicas are simultaneously maintained, with harmonic restraints enforcing the average $\langle \ln \mathrm{PF}_i \rangle = \beta_c \langle N_c \rangle_i + \beta_h \langle N_h \rangle_i$ calculated across all the simulation replicas. All-atom simulations of chymotrypsin inhibitor 2 (CI2) restrained by this method yield conformational ensembles consistent with experiment.

One problem with restraint simulations is the risk of introducing unnecessary bias into the ensemble from the restraint potential. Pitera and Chodera have used a maximum entropy approach to show that the least-biased method to restrain some ensemble-averaged quantity $\langle f(x) \rangle$, where $f(x)$ is a structural observable computed for a conformation, x, is to use a modified force field potential $U(x) = U(x) + \alpha f(x)$, for some scaling parameter α.[19] In practice, the value of α can be determined by performing multiple simulations at different values of α, and selecting the value that reproduces the correct value of $\langle f(x) \rangle$. In the limit of large numbers of replicas, the Vendroscolo et al. method approaches this maximum entropy solution. The maximum entropy method has a practical drawback, however: using it to restrain protection factors for a large number of amino acids in a protein would require exploring an enormously large parameter space. As we show below, we can alternatively use a simplified version of this idea to simulate ensembles more consistent experimental protection factors.

Overview

In this manuscript, we expand on previous work in several ways. Our results are organized into three parts. In Part I, we take a Bayesian inference approach to parameterizing an empirical predictor of HDX protection factors from molecular simulation data. Starting with a functional form similar to Vendruscolo et al., we fit against newly-available ultra-long molecular simulation trajectory data, while retaining the full posterior distribution of model parameters. In Part II, we pursue a new way of performing biased simulations to generate structural ensembles consistent with HDX protection factor data, through the example of apomyoglobin (apoMb). Inspired by the maximum entropy method of Pitera and Chodera,[19] we perform simulations of apoMb using a number of different bias potentials and temperatures, and use the resulting trajectory data to construct multi-ensemble Markov State Models.[20] In Part III, we use a Bayesian inference approach, implemented through our BICePs (Bayesian Inference of Conformational Populations) algorithm,[21,22] to reconcile the MSMs built for each thermodynamic ensemble against experimental protection factor measurements and chemical shift measurements. The key advantage of this approach is that we can use Bayesian inference to propagate uncertainty in model parameters (found in the first part) to perform quantitative model selection.

Methods and Results

Part I: An empirical model of HDX protection parameterized from ultra-long simulation trajectory data

We first attempted to construct a new empirical model–trained on ultra-long MD trajectories–to predict protection factors according to the following form:

$$\ln \mathrm{PF}_i = \beta_c \langle N_c \rangle_i + \beta_h \langle N_h \rangle_i + \beta_0, \tag{2}$$

This form is similar to the Vendruscolo et al. model,[13] but with an additional cooperativity term β_0 that can compensate for the correlations between heavy-atom contacts and hydrogen-bond contacts.

The values of the parameters for this model come from fitting to ultra-long (millisecond) native-state molecular dynamics simulations of the 58-residue protein BPTI,[15] and the 76-residue protein ubiquitin,[16] both provided by D.E. Shaw Research. First, we will describe the simulation trajectory data sets, and later describe our parameterization scheme, in which we use Bayesian inference to compute the full posterior distribution of likely parameters.

BPTI and ubiquitin molecular dynamics trajectory data. From each simulation, we procured a sample trajectory of 50000 snapshots for model parameterization, typical of conventional explicit-solvent simulation trajectories. The native-state BPTI simulation was performed at 300 K with 4215 water molecules, from which we analyzed a segment of the full trajectory (71-83.5 μs) containing 50000 frames taken every 250 ps. The native-state ubiquitin simulation was performed at 300 K with 5581 water molecules, from which we analyzed a trajectory of 50000 snapshots taken every 20 ns. The RMSD variances on the native state ensembles of both systems is small (Figure 1), and thus can be used to study hydrogen exchange in native states.

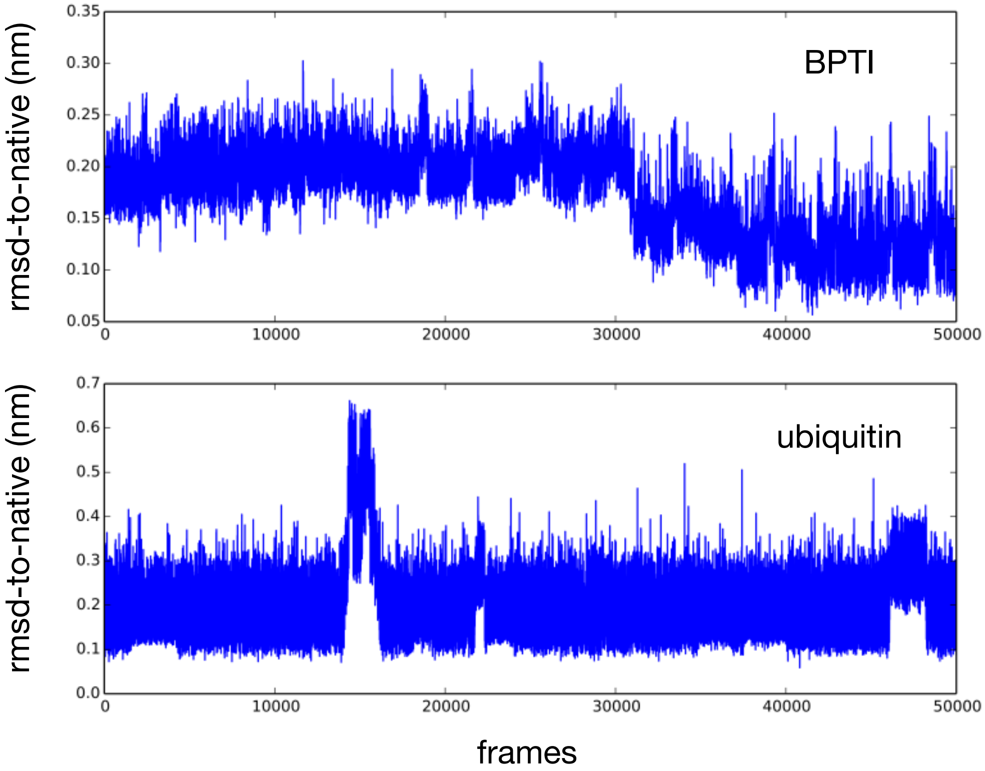

Figure 1: Molecular dynamics trajectory data used for training an empirical model of HDX protection. Shown is rmsd-to-native over time for 50000 frames of BPTI (frames every 250 ps) ubiquitin (frames every 20 ns). Trajectory data was provided by D.E. Shaw Research.

Bayesian model parameterization. In addition to the scaling parameters β_c, β_h, and β_0 in Equation (2), there are parameters associated with how the average numbers of heavy-atom contacts $\langle N_c \rangle_i$ and hydrogen-bonds $\langle N_h \rangle_i$ are computed for each residue i. The averages are calculated using sigmoidal cut-off functions averaged over all T snapshots in the sample. $\langle N_c \rangle_i$ is computed as

$$\langle N_c \rangle_i = \frac{1}{T} \sum_{t=1}^{T} \sum_{j} \frac{e^{-b(x_{ij}(t)-x_c)}}{1+e^{-b(x_{ij}(t)-x_c)}}, \qquad (3)$$

where $x_{ij}(t)$ are the distances (in Å) from the backbone amide nitrogen of residue i to other heavy atoms j, at snapshot t, and x_c is a distance threshold parameter defining a heavy-atom contact. Similarly, $\langle N_h \rangle_i$ is computed as:

$$\langle N_h \rangle_i = \frac{1}{T} \sum_{t=1}^{T} \sum_{k} \frac{e^{-b(x_{ik}(t)-x_h)}}{1+e^{-b(x_{ik}(t)-x_h)}}, \tag{4}$$

where $x_{ik}(t)$ are the distances (in Å) between the backbone amide hydrogen of residue i to oxygen hydrogen-bond acceptors k, at snapshot t, and x_h is a distance threshold parameter defining a hydrogen bond. The parameter b has units Å^{-1} and controls the sharpness of the sigmoidal cutoff for both $\langle N_c \rangle_i$ and $\langle N_h \rangle_i$. Taken together, there are six parameters in our model to be inferred from the training data: $\beta_c, \beta_h, \beta_0, x_c, x_h$, and b.

To determine these parameters, we implement a Bayesian inference approach. While traditional optimization schemes aim to find a particular set of parameters that maximize a likelihood function, Bayesian approaches aim to sample the entire posterior distribution of parameters $\lambda = (\beta_c, \beta_h, \beta_0, x_c, x_h, b)$, from which uncertainty estimates can be computed. By Bayes theorem, the posterior probability distribution $P(\lambda|D)$ of parameters, given some experimental data D, obeys the proportionality

$$P(\lambda|D) \propto P(D|\lambda,\sigma)P(\lambda)P(\sigma) \tag{5}$$

where $P(D|\lambda)$ is a likelihood function describing the probability of observing the data given the parameters, and $P(\lambda)$ is a prior distribution of parameters, which we set to be uniform in some reasonable range. For our likelihood function, we use a Gaussian error function

$$P(D \mid \lambda) = \prod_{i}^{n_{\mathrm{res}}} (2\pi\sigma^2)^{-1/2} e^{-(\Delta \ln \mathrm{PF}_i)^2/2\sigma^2} \tag{6}$$

where $\Delta(\ln \mathrm{PF}_i)$ are the differences in experimental and predicted protection factors, n_{res} is the number of residues, and σ is a parameter specifying the expected error. Since the expected error is unknown, we include σ as a nuisance parameter in the posterior distribution,

$$P(\lambda, \sigma|D) \propto P(D|\lambda, \sigma)P(\lambda)P(\sigma) \tag{7}$$

with $P(\sigma) \sim \sigma^{-1}$ chosen to be an uninformative Jeffreys prior.

Training the model. The experimental data used to train the model included: (1) 72 experimental protection factors for ubiquitin compiled by Craig et al. as the average of rescaled HDX data studied at different pH,[23] and (2) experimental protection factors for 30 of the 53 amide hydrogens of BPTI with published NMR HDX measurements at 300 K.[24–27] These 30 were the same set used by Persson and Halle, in which the authors excluded highly protected amides and surface amides which exhibited anomalous pH dependence.[17] A full list of experimental protection factors, converted to $\ln \mathrm{PF}$ values, are listed in the Supporting Information (Tables S1 and S2).

Training the model entails sampling the full posterior $P(\lambda, \sigma|D)$ over all model parameters $(\lambda = (\beta_c, \beta_h, \beta_0, x_c, x_h, b), \sigma)$ using random walk Monte Carlo sampling. At each step, one of these seven variables was randomly chosen and a move was proposed to a new nearest-neighbor on a grid of allowed values, and accepted with the Metropolis criterion. Values of β_c ranged from 0.05 to 0.20 kT in increments of 0.01 kT. Values of β_h ranged from 0 to 5.0 kT in increments of 0.2 kT. Values of β_0 ranged from -10 to 0 kT in increments of 0.2 kT. Values of x_c ranged from 5.0 to 8.0 Å in increments of 0.5 Å. Values of x_h ranged from 2.0 to 2.7 Å in increments of 0.1 Å. Values of b ranged from 3 to 20 Å^{-1} in increments of 1 Å^{-1}. The value of σ was constrained to 100 log-spaced grid values from 0.25 to 5.0. Using these values, all variables had acceptance ratios greater than 0.50. Trials of 10^6 and 10^7 steps were performed, with similar results (see below).

The marginal distribution of $P(\lambda|D)$ is obtained through $\int P(\lambda, \sigma|D)d\sigma$. Posterior marginal distributions for each parameter are calculated similarly, from the values sampled by Monte Carlo (Figure 2). To ensure robust results, we trained the model separately on ubiquitin (Figure 2a) and BPTI (Figure 2b), and also on both data sets (Figure 2c).

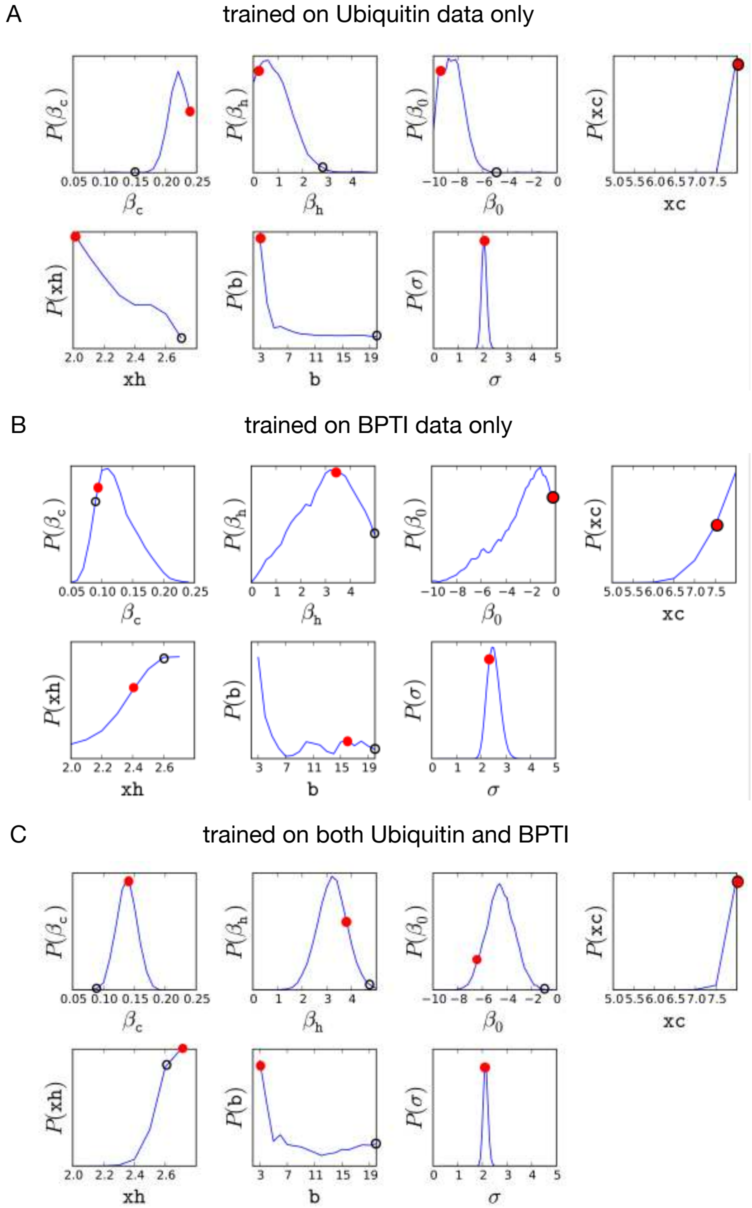
A trained on Ubiquitin data only

B trained on BPTI data only

C trained on both Ubiquitin and BPTI

Figure 2: Posterior marginal distributions of model parameters $\beta_c \beta_h, \beta_0, x_c, x_h, b$, and σ, obtained from Monte Carlo sampling. Parameters $\beta_c \beta_h, \beta_0$ are in units kT. Parameters x_c and x_h have units Å. The parameter b (units Å^{-1}) controls the sharpness of the sigmoidal cutoff for determining the presence of a heavy-atom contact or hydrogen bond, and σ represents the standard error in predicting $\ln \mathrm{PF}_i$.

The posterior distributions of model parameters are similar when trained individually on ubiquitin or BPTI protection factors alone, but differences can be observed, mainly in the importance of heavy-atom coordination versus hydrogren bonds. Whereas the ubiquitin-

Table 1: Maximum likelihood (ML) and maximum a posteriori (MAP) model parameters for a $\ln \mathrm{PF}_i$ predictor trained on ubiquitin data only (Ubq).

	ML	MAP (10^6 samples)	MAP (10^7 samples)
${\beta_c}^a$	0.15	0.24	0.23
${\beta_h}^a$	2.8	0.2	0.4
${\beta_0}^a$	-5.0	-9.6	-9.0
${x_c}^b$	8	8	8
${x_h}^b$	2.7	2.0	2.7
b^c	20	3	3
σ		2.097	2.036
SSE^d	470.00	563.99	550.87
rms^e	2.555	2.799	2.766

^{a} units kT; ^{b} units Å; ^{c} units Å^{-1}; ^{d} sum of squared errors over 72 ubiquitin residues; ^{e} root mean squared deviation.

Table 2: Maximum likelihood (ML) and maximum a posteriori (MAP) model parameters for a $\ln \mathrm{PF}_i$ predictor trained on BPTI data only (BPTI).

	ML	MAP (10^6 samples)	MAP (10^7 samples)
${\beta_c}^a$	0.08	0.09	0.07
${\beta_h}^a$	5.0	3.4	4.0
${\beta_0}^a$	-0.2	-0.2	-1.8
${x_c}^b$	7.5	7.5	8.0
${x_h}^b$	2.6	2.4	2.7
b^c	20	16	3
σ		2.227	2.227
SSE^d	221.03	267.58	272.00
rms^e	2.714	2.986	3.011

^{a} units kT; ^{b} units Å; ^{c} units Å^{-1}; ^{d} sum of squared errors over 30 BPTI residues; ^{e} root mean squared deviation.

trained model has a large β_c coefficient and a low β_h coefficient (with a lower distance threshold x_h for including hydrogen bonds), the opposite is true for the BPTI-trained model. The model trained on both data sets has posterior distributions centers on intermediate values of β_c and β_h.

Of all the possible sets of parameters sampled in the full posterior distribution, it is useful to pick a single set of parameters to formulate a $\ln \mathrm{PF}_i$ predictor. We do this by choosing the maximum a posteriori (MAP) parameter values $\lambda^* = \mathrm{argmax}\ P(\lambda|D)$, i.e. the parameters that give the maximum value of the joint posterior distribution. The MAP is

Table 3: Maximum likelihood (ML) and maximum a posteriori (MAP) model parameters for a $\ln \mathrm{PF}_i$ predictor trained on both ubiquitin and BPTI data (Ubq+BPTI).

	ML	MAP (10^6 samples)	MAP (10^7 samples)
$\beta_c{}^a$	0.08	0.14	0.14
$\beta_h{}^a$	4.6	3.8	3.4
$\beta_0{}^a$	-1	-6.2	-5.8
$x_c{}^b$	8.0	8.0	8.0
$x_h{}^b$	2.6	2.7	2.7
b^c	20	3	3
σ		2.161	2.161
SSE^a	764.25	872.10	866.14
rms^b	2.737	2.924	2.914

^{a} units kT;x ^{b} units Å; ^{c} units Å^{-1}; ^{d} sum of squared errors over 102 residues; ^{e} root mean squared deviation.

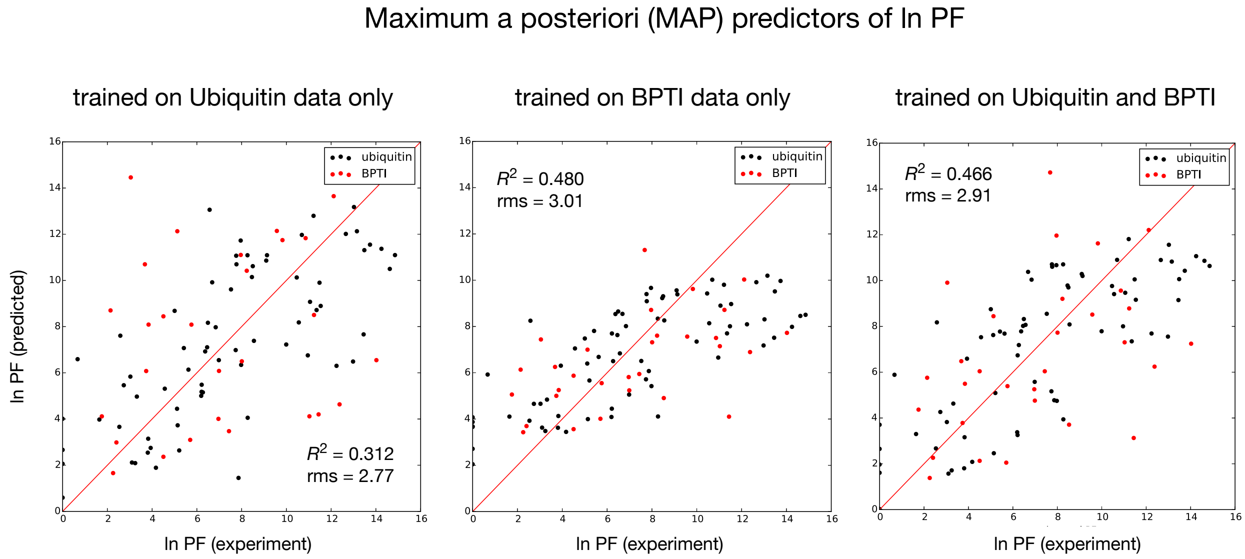

Figure 3: Comparisons of experimental and predicted values of $\ln \mathrm{PF}_i$ from maximum a posteriori (MAP) models trained on ubiquitin data only (Ubq), BPTI data only (BPTI), and both data sets (Ubq+BPTI). Values of R^2 and rms values reported in each subplot are for the entire dataset (Ubq+BPTI)

distinguished from the maximum likelihood (ML) parameters, which are the set of parameters that minimize the likelihood function in Equation 6. Because this likelihood function is a Gaussian error function, it is minimized when sum of squared errors (SSE) $\sum_i \Delta \ln \mathrm{PF}_i$ is minimized. Thus, the ML model is comparable to a linear regression model where the sum of squared residuals are minimized. Such models can be overly sensitive to outliers, a problem which can be ameliorated with the use of a Bayesian posterior. Indeed, we find that the ML model (black circles in Figure 2) parameters are located in the tails of the posterior distribution, unrepresentative of the larger posterior distribution. Moreover, we also note that, because the parameters are not independent, the maximum a posteriori (MAP) set of parameters $\lambda^* = \text{argmax}\ P(\lambda|D)$ (red filled circles in Figure 2) is *not* the maximum of each marginal posterior distribution.

ML and MAP parameters λ^* for ubiquitin-trained (Ubq) and BPTI-trained models (BPTI) are shown in Tables 1 and 2, respectively. ML and MAP parameters λ^* for models trained on both data sets (Ubq+BPTI) are shown in Table 3. To test whether we have adequately sampled the posterior distribution, we compare the results when using 10^6 and 10^7 MCMC samples; the results are extremely similar in all cases. The rms errors in the $\ln \text{PF}_i$ predictions from MAP are not that much larger than those for the ML models (which by definition give the lowest rms errors): whereas the Ubq, BPTI and (Ubq+BPTI) ML models yield rms errors in $\ln \text{PF}_i$ of 2.555, 2.714 and 2.737, respectively, the MAP models have rms only slightly larger: 2.766, 3.011 and 2.914, respectively (using 10^7 MCMC samples). For both the ML and MAP models, training on both sets of data (Ubq+BPTI) yields rms errors similar to models trained on each protein alone (Ubq, or BPTI).

When we use the MAP λ^* of Ubq-, BPTI- and (Ubq+BPTI)-trained models to compare experimental and predicted values of $\ln \text{PF}_i$ (Figure 3), we find squared correlation coefficient R^2 values of 0.312, 0.480 and 0.466, respectively. Since the (Ubq+BPTI)-trained MAP model exhibits the best balance of low rms error and high R^2 values, and uses all the available training data, we use this model for all subsequent work (see Part III). The R^2 value of this model is comparable to Craig et al.'s prediction on ubiquitin ($R^2 = 0.53$) and Persson and Halle's predictions for BPTI ($R^2 = 0.68$). The lower extent of correlation for our PF predictions may arise in part from our smaller training set of molecular simulation data. Only 5×10^4 frames were used to train our model, versus 10^6 frames used in Halle's predictions on BPTI, and 2×10^5 frames for Craig's prediction on ubiquitin.

The values of β_c and β_h in our final MAP (Ubq+BPTI) model (Table 3, 10^7 steps) can be used to gain insight into the unfolding (closed-to-open state) free energy contributions provided by heavy-atom contacts and hydrogen bonds, through the terms $\beta_c \cdot \langle N_c \rangle_i$ and $\beta_h \cdot \langle N_h \rangle_i$, respectively, for each residue i (Figure 4). These values range from contributions of 4–16 kT attributed to heavy-atom contacts, and 1–6 kT attributed to hydrogen bond breaking, depending on the residue. These two free energy contributions are correlated, as indicated by the cooperativity term of β_0 = -5.8 kT. This term provides a correction factor to offset the "double-counting" of these related contributions. These results are similar to the results of Vendruscolo et al., who estimated (uncorrelated) free energy contributions of 0.6 kcal mol^{-1} ($\sim$1 kT) per heavy-atom contact, and 3 kcal mol^{-1} ($\sim$5 kT) per hydrogen bond.[13]

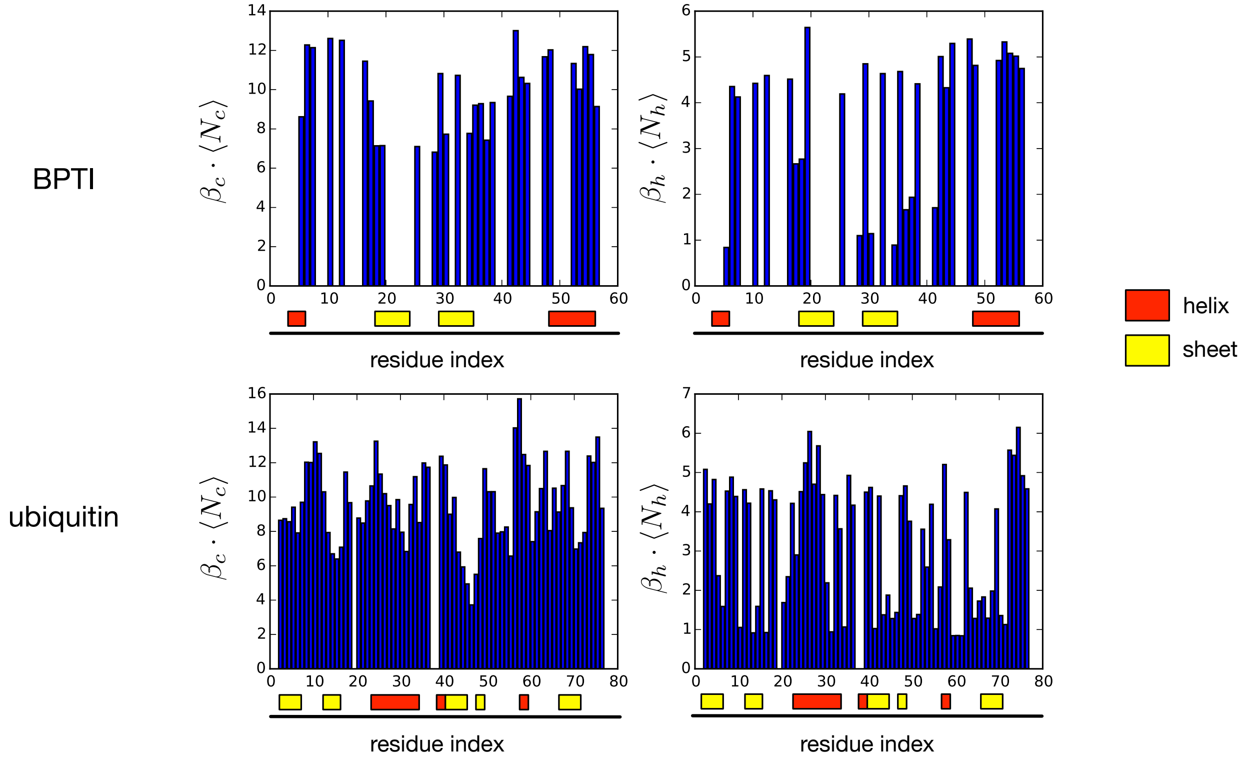

Figure 4: Estimates of the unfolding (closed-to-open state) free energy contributions (in units kT) originating from heavy-atom contacts $\beta_c \cdot \langle N_c \rangle_i$, versus hydrogen bonding $\beta_h \cdot \langle N_h \rangle_i$ for each residue i, according to the MAP predictor of $\ln \mathrm{PF}_i$.

Part II. Restraint-biased simulation and construction of multi-ensemble MSMs for apoMb

From our work above, we now have in hand a reasonably accurate function, $\ln \mathrm{PF}_i(X) = \beta_c \langle N_c \rangle_i(X) + \beta_h \langle N_h \rangle_i(X) + \beta_0$, that yields a prediction of $\ln \mathrm{PF}_i$ for residue i, given a molecular conformation X. According to the maximum entropy approach of Pitera and Chodera,[19] the least-biased potential to restrain protection factor observables in a molecular simulation is expressed as a modified potential $U'(X) = U(X) + \sum_i \alpha_i (\ln \mathrm{PF}_i(X))$. This would require performing an unfeasible number of simulations to explore the full parameter space of all α_i.

Instead, we propose a simplification to this scheme, in which a single restraint bias potential (with a single parameter α), is applied to multiple protein residues, so as to generate structural ensembles with different extents of solvent exposure and amide hydrogen bonding. Later (as we describe below), the ensembles will be evaluated using the BICePs algorithm to determine which is most consistent with the experimental data.

Apomyoglobin. As a specific system on which to test this approach, we consider apomyoglobin (apoMb), a protein whose folding has been well-studied by NMR and x-ray crystallography.[28,29] Myoglobin is a 152-residue heme protein with eight helices labeled A through H (Figure 5). In the absence of heme at pH 6, apomyoglobin adopts a holoprotein-like conformation, although the F helix and C-terminal portion of the H helix becomes disordered.[30,31] This conformation is known as the *native* (N) state of apoMb. At pH 4.0, apomyoglobin becomes more highly disordered; this acid-denatured state (M) is similar to a kinetic intermediate in the refolding of apoMb, as characterized by quench-flow amide proton H/D exchange pulse labeling and stopped-flow spectroscopy.[32–36]

Here, we focus on generating simulated ensembles of apoMb that best represent the N state of apoMb. Our primary goal is to reconcile the ensembles against protection factors for apomyoglobin at pH 6.0 and pH 4.0 measured by Nishimura et al.[37] and NMR chemical shifts measured by Eliezer and Wright.[30]

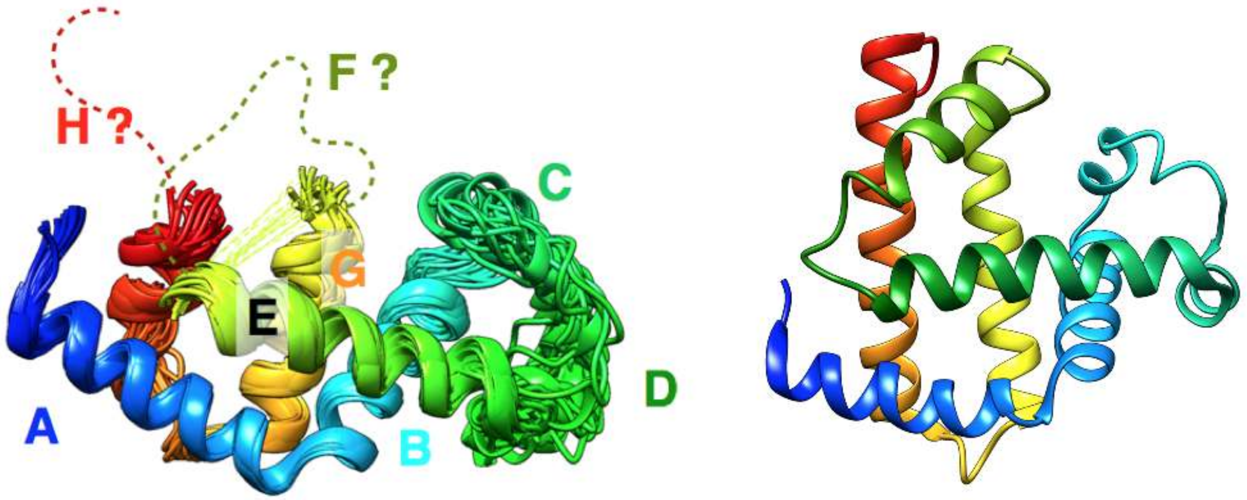

Figure 5: (Left) NMR structure of apomyoglobin at neutral pH shows disordered F and H helices (Lecomte 1999, personal communication). (Right) Holo-myoglobin (PDB:1JP6) was the starting conformation of the restraint-bias molecular simulations.

Molecular simulation. Molecular simulations of apomyoglobin were prepared and performed using the GROMACS 5.0.1 simulation package on TACC Stampede supercomputer. NVT simulations were performed using a stochastic (Langevin) integrator with step size 2 fs. The AMBER ff99SB-ildn-nmr force field and TIP3P water model were used with cubic periodic box of volume (6.743 nm)^3 containing 30072 atoms, which included the protein, 9194 water molecules, 18 Na$^+$ ions, and 20 Cl$^-$ ions (approximately 100 mM salt concentration).

The starting conformation of the protein was taken from holomyoglobin (PDB:1JP6). Protonation states at pH 7 were chosen according to the pKa values measured by Geierstanger et al.[32]

Restraint bias potentials to encourage solvent exposure. To encourage the solvent-exposure of specific residues, sigmoidal restraint bias potentials were included in the simulations (Figure 6). The restraint biases were implemented using tabulated bonded interactions (cubic spline potentials) in GROMACS, of the form $U_{\text{bias}}(x) = k \cdot f(x)$, where k is a force constant in units of energy, and $f(x)$ is a function of interatomic distance x,

$$f(x) = \frac{e^{-b(x-x_0)}}{1+e^{-b(x-x_0)}}, \tag{8}$$

where $x_0 = 0.65$ nm, and $b = 5$ nm^{-1}.

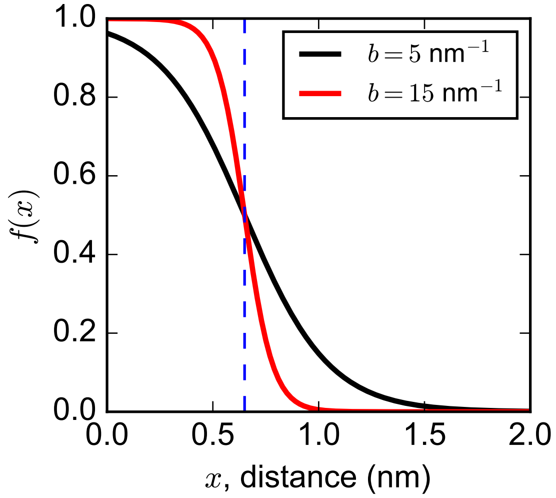

Figure 6: The sigmoidal function $f(x)$ used with the biasing potential $U_{\text{bias}}(x) = k \cdot f(x)$, where k is a force constant in units of energy. The value of b was set to 5 nm^{-1}.

Protection factors for apoMb measured by Nishimura et al.[37] show that helix F and the C-terminal region of helix H are more solvent-exposed for apoMb than the *holo* protein. Therefore, bias restraints were added between the amide hydrogens of in helix F (residues 83-87, 89-95), and helix H (residues 140-152) and oxygens on all residues capable of making hydrogen bonds; these included backbone carbonyl oxygens, as well as side chain oxygen atoms on aspartic acid, glutamic acid, glutamine, serine, threonine and tyrosine (Figure 7).

Simulations were performed at temperatures 300, 330, 350, 370, 400 and 415 K. For each temperature, simulations were performed using force constants of $k = 0.5, 0.7, 1.0, 1.2, 1.5$ and 2.0 kJ, resulting in 36 simulations totalling 19 μs of aggregate simulation trajectory data (Table 4), with snapshots saved every 100 ps.

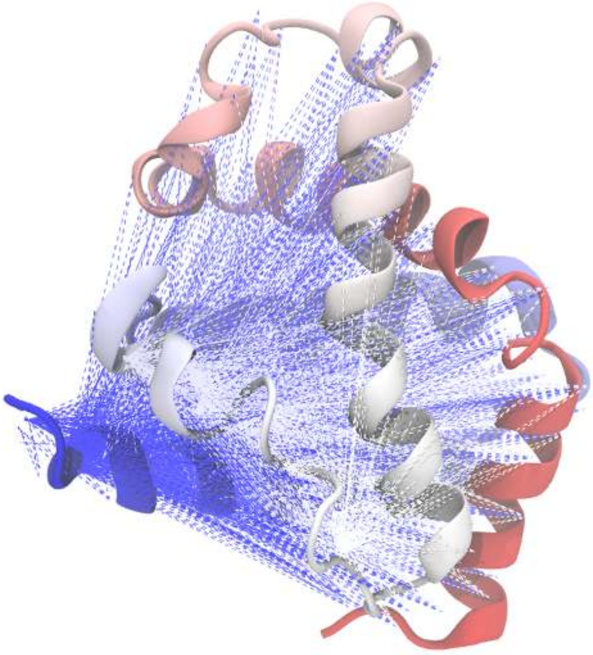

Figure 7: Visualization of protection factor restraints applied to selected residues of apoMb.

Table 4: A summary of molecular dynamics simulation trajectory data for apoMb.

	trajectory length (in μs)					
force constant (kJ)	300 K	330 K	350 K	370 K	400 K	415 K
0.0	15.7	6.2	5.9	5.6	6.2	6.0
0.5	1.0	1.0	1.0	0.8	0.08	0.08
0.7	1.0	1.0	1.0	0.8	0.08	0.08
1.0	1.0	1.0	1.0	0.07	0.08	0.08
1.2	1.0	1.0	1.0	0.7	0.08	0.08
1.5	1.0	1.0	1.0	0.08	0.08	0.08
2.0	0.6	1.0	1.0	0.08	0.08	0.08

Construction of multi-ensemble MSMs from restraint-biased trajectory data

The simulation trajectory data obtained at multiple temperatures and restraint-bias potentials were next used to construct multi-ensemble Markov Models (MEMMs). These models can be thought of as a *set* of MSMs–one for each thermodynamic ensemble. The main advantage of MEMMs is that observed transitions sampled across all the ensembles can provide information to estimate transition rates between states in each individual ensemble.

Projection of trajectory data to discrete metastable states. Discretization of the trajectory data for MSM analysis was accomplished by first performing dimensionality reduction of the coordinate data, and then conformational clustering in the low-dimensional projection to define metastable states.

Time-lagged independent component analysis (tICA)[38,39] was used to determine the low-dimensional subspace corresponding to the slowest motions of the protein. Similar to principal component analysis (PCA), which finds the eigenvectors of a covariance matrix, the tICA method solves a similar eigenvalue problem for a time-lagged correlation matrix to find the degrees of freedom that capture the most time-correlated motions. As input coordinates, we used all pairwise distances between C_α atoms. The tICA lag time used was 0.5 ns. The entire set of trajectory data (all temperatures and force constants) was used as input to tICA.

Next, the trajectory data were projected to the top 8 tICA components, and k-centers clustering was performed in this subspace to identify 25 microstates with which MSMs (and MEMMs) could be constructed (Figure 8). The number of microstates was chosen to facilitate sufficient overlap of metastable states to construct MEMMs (as described below). Visualization of the trajectory data on tIC_1 and tIC_2 shows that the slowest motion (moving left to right along tIC_1) corresponds to the unstructuring of helix F and helix H. Microstate 16 (microstates are numbered using indices 0 through 24) on the left side of Figure 8a is the state from which all trajectories were initiated, a *holo*-like structure with a folded F-helix and an rmsd of 0.25 nm to the native structure. On the right side of Figure 8a are a number of microstates corresponding to conformational states lacking structure in helix F and H.

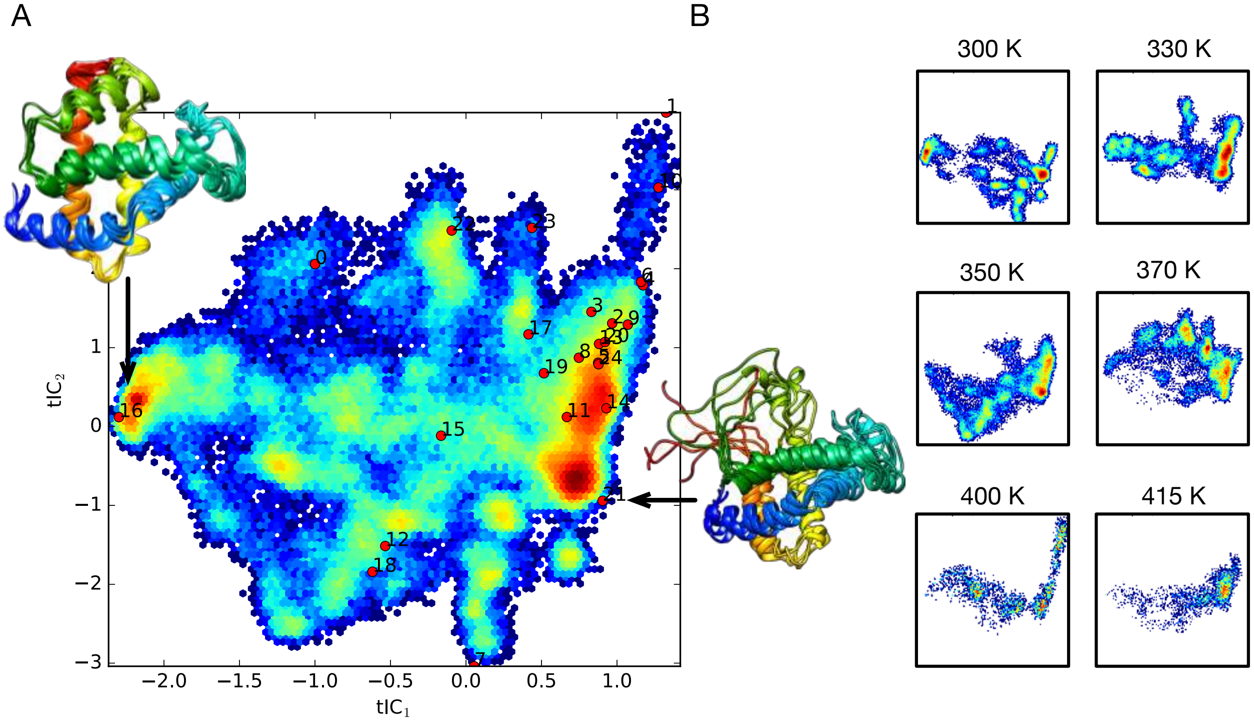

Figure 8: Visualization of apoMb trajectory data on the tICA landscape. (A) A density map of trajectory data from all temperatures and force constants projected to tIC$_1$ and tIC$_2$. Red dots indicate the centers of the conformational clusters used as MSM metastable states, labeled by microstate index. (B) Density maps of trajectory data for the six simulation temperatures, shown separately on the same axes as panel A.

Construction of MEMMs. The TRAM (transition-based reweighting analysis method) algorithm,[20] as implemented in the PyEMMA software package,[40] was used to construct multi-ensemble Markov Models of apoMb from the simulation trajectory data. TRAM uses information from a series of thermodynamic ensembles, labeled by index k, to infer both the transition rates $p_{ij}^{(k)}$ between states i and j in ensemble k and the conformational (reduced) free energies $f_i^{(k)}$ of each state i in ensemble k. This is achieved by maximization of a joint likelihood function L_{TRAM} that is the product of a reversible MSM estimator likelihood function $L_{\mathrm{MSM}}^{(k)}$, and a free energy estimator likelihood function $L_{\mathrm{LEQ}}^{(k)}$:

$$L_{\mathrm{TRAM}} = \prod_{k=1}^{K} \underbrace{\left(\prod_{i,j} (p_{ij}^{(k)})^{c_{ij}^{(k)}} \right)}_{L_{\mathrm{MSM}}^{(k)}} \underbrace{\left(\prod_{i=1}^{m} \prod_{x \in X_i^{(k)}} \mu(x) e^{f_i^{(k)} - b^{(k)}(x)} \right)}_{L_{\mathrm{LEQ}}^{(k)}} \tag{9}$$

where $c_{ij}^{(k)}$ are the number of transition counts between states i and j observed in ensemble k, $\mu(x)$ is the normalized equilibrium probability ($\sum_x \mu(x) = 1$) of each sample x, $X_i^{(k)}$ is the set of samples x drawn from the k^{th} ensemble, and $b^{(k)}(x)$ is the (reduced) bias potential acting on sample x in ensemble k.

Due to insufficient overlap of sampled conformational states across the simulated temperatures, MEMMs were constructed for each temperature, using all simulation trajectory data obtained at all viable restraint biases. For example, for simulations performed at 350 K, a total of four restraint-biased ensembles were included in the TRAM estimation, for force constant values of $k = 0.5$, 0.7, 1.0, and 1.2 kJ. The key quantity of interest resulting from these calculations are the equilibrium populations of conformational states.

We projected the 350 K trajectory data from each microstate onto tIC_1 after weighting by its estimated population, to obtain a series of free energy profiles $F^{(k)}(\mathrm{tIC}_1) = -k_B T \ln \pi^{(k)}(\mathrm{tIC}_1)$ for each thermodynamic ensemble k. All free energy profiles show two minima separated by a 2–4 kcal mol^{-1} barrier, with the global minimum shifting from structured conformations to unstructured conformations for helix F as the force constant increases (Figure 9). This clearly shows how the restraint biases are able to achieve a range of conformational distributions which we can reconcile against experimental measurements.

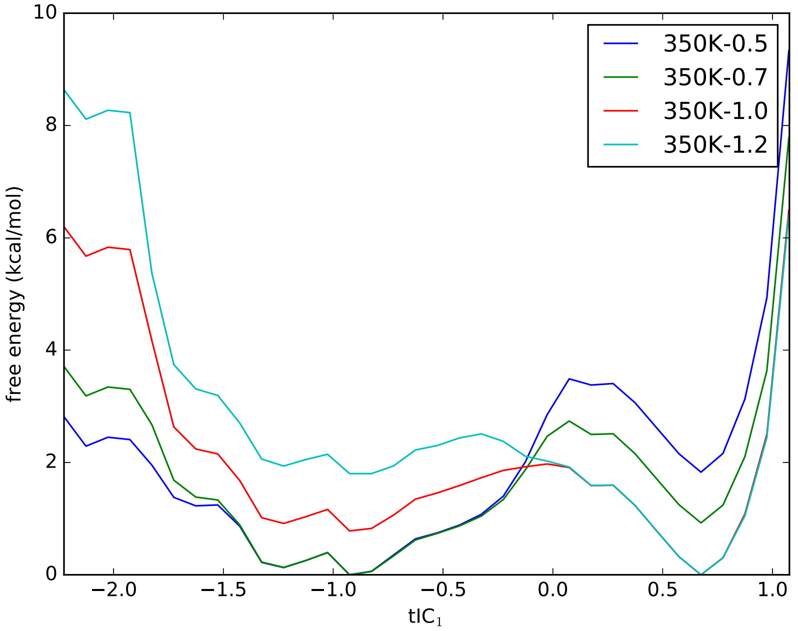

Figure 9: TRAM predictions of free energy profiles along tIC_1 for ensembles at 350 K and with biases of $k = 0.5, 0.7, 1.0,$ and 1.2 kJ.

Part III: Reconciling multi-ensemble MSMs against experimental HDX protection factor and chemical shifts data using BICePs

From the work described in the previous section (Part II), we now have in hand a series of MSMs for each thermodynamic ensemble (defined by a particular temperature and restraint bias), each yielding a prediction of equilibrium conformational populations. From the work described in Part I, we also have in hand a predictor of the observable ($\ln \text{PF}_i$) for each conformational state X,

$$\ln \text{PF}_i(X|\lambda) = \beta_c \langle N_c \rangle_i (X|x_c, b) + \beta_h \langle N_h \rangle_i (X|x_h, b) + \beta_0, \qquad (10)$$

along with the full posterior $P(\lambda)$ of nuisance parameters $\lambda = (\beta_c, \beta_h, \beta_0, x_c, x_h, b)$.

Using these two ingredients, we now proceed to reconcile each MSM against the experimentally measured observables. Specifically, we wish to find the set of MSM-predicted conformational populations that best agrees with the experimental observables. To do accomplish this task, we take a Bayesian inference approach, implemented through an algorithm we call Bayesian Inference of Conformational Populations, or BICePs.

The BICePs algorithm

For a full discussion of the background and development of BICePs, please refer to our previous work.[21,22,41,42]

The purpose of BICePs is to make unbiased estimates of conformational populations by optimally combining information from theoretical predictions (here, all-atom simulations) and ensemble-averaged experimental observables. The goal is to sample the posterior probability distribution of conformational states X, given some experimental data D. By Bayes' Theorem,

$$P(X \mid D) \propto P(D \mid X)P(X) \tag{11}$$

where $P(D \mid X)$ is a likelihood function representing experimental restraints, and $P(X)$ is a prior probability function, calculated from a theoretical model (in this case, from molecular simulation). BICePs is similar to other Bayesian methods for the inference of structural ensembles, including ISD,[43] MELD,[44] and Metainference.[45]

Nuisance parameters. One important feature of BICePs is the ability to infer how best to balance the relative influence of experimental versus theoretical restraints. It does this by modeling the (unknown) uncertainty of the experimental measurements and heterogeneity in the conformational ensemble using nuisance parameters σ, and sampling over these parameters to estimate their posterior distribution as well, through

$$P(X, \sigma \mid D) \propto P(D \mid X, \sigma)P(X)P(\sigma) \tag{12}$$

where we assume some prior distribution $P(\sigma)$.

Reference potentials. Another important feature of BICePs is the use of reference potentials. An experimental observable $r(X)$ is a projection of a high-dimensional conformational ensemble X to a single-valued function, and therefore the likelihood $P(D \mid X, \sigma)$ of observing a particular value $r(X)$ must be expressed relative to some reference probability $P_{\text{ref}}(r(X))$ of observing $r(X)$ in the absence of any particular structure, according to

$$P(X, \sigma \mid D) \propto \left[\frac{P(r(X) \mid D, \sigma)}{P_{\text{ref}}(r(X))} \right] P(X) P(\sigma) \tag{13}$$

BICePs scores for unbiased model selection. As discussed by Ge et al.,[22] another advantage of BICePs is its ability to perform model selection. Given a set of conformational populations predicted by an MSM, we wish to objectively evaluate the extent to which it agrees with experimental observables, and be able to rank it against other models.

Suppose we are presented with a collection of competing models $P^{(k)}(X, \sigma \mid D)$, each with a different theoretical prior $P^{(k)}(X)$ predicted from an MSM. The total evidence for model $P^{(k)}$ can be expressed as

$$Z^{(k)} = \int P^{(k)}(X, \sigma \mid D) dX d\sigma = \int P^{(k)}(X) Q(X) dX, \tag{14}$$

where $Q(X) = \int [P(r(X) \mid D, \sigma)/P_{\text{ref}}(r(X))] P(\sigma) d\sigma$ represents the probability of X given the experimental data. As can be seen by the last term in Equation (14), $Z^{(k)}$ is an overlap integral that quantifies how well the theoretical $P^{(k)}(X)$ agrees with the experimental data.

To compare two different models $P^{(1)}$ and $P^{(2)}$, it is common to compute the ratio of total evidences, $Z^{(1)}/Z^{(2)}$, often called the *Bayes factor*. To facilitate the assignment of a unique score to each model, we compute a Bayes factor where the second model is a "null" model Z_0 in which $P^{(k)}(X)$ is a uniform distribution of conformational states. In this way, we define a quantity we call the BICePs score, $f^{(k)}$, for each model $P^{(k)}$,

$$f^{(k)} = -\ln \frac{Z^{(k)}}{Z_0}. \tag{15}$$

In practice, the calculation of the BICePs score $f^{(k)}$ can be performed using free energy estimation techniques, and can be thought of as a "free energy" of each model $P^{(k)}$; the lower the value of $f^{(k)}$, the better the model agrees with the experimental data. We can thus use the BICePs score $f^{(k)}$ for objective model selection. We use the multistate Bennett acceptance ratio (MBAR) method[46] was used to calculate the BICePs scores $f^{(k)}$.

Reconciling conformational populations of apoMb against experimental observables using BICePs

Here, we use two kinds of experimental data with the BICePs algorithm: HDX protection factors measured by Nishimura et al.,[37] and NMR chemical shifts for H, C_α, and N atoms measured by Eliezer and Wright.[30] Experimental protection factor data for apoMb, converted to $\ln \mathrm{PF}$ values, are listed in the Supporting Information (Table S3).

Protection factor restraints. For each residue i, we introduce a Gaussian function to restrain the computed observable $r_i(X) = \ln \mathrm{PF}_i(X)$, against the measured values r_i^*,

$$P(r_i^* \mid X, \lambda, \sigma_{\mathrm{PF}}) = \frac{1}{\sqrt{2\pi\sigma_{\mathrm{PF}}^2}} \exp(\frac{-(r_i^* - \ln \mathrm{PF}_i(X \mid \lambda, \sigma_{\mathrm{PF}}))^2}{2\sigma_{\mathrm{PF}}^2}), \tag{16}$$

where σ_{PF} represents the uncertainty in the experimental measurement, and $\lambda = (\beta_c, \beta_h, \beta_0, x_c, x_h, b)$. As in previous BICePs calculations,[21,42] we used exponential reference potentials $P_{\mathrm{ref}}(r_i(X))$ for all residues i, and an uninformative Jeffreys prior $P(\sigma_{\mathrm{PF}}) \sim \sigma_{\mathrm{PF}}^{-1}$. The prior distribution $P(\lambda)$ comes from the posterior distribution of the nuisance parameters sampled in Part I (see Figure 2).

Chemical shift restraints. For each residue i, we introduce a Gaussian function to restrain predicted chemical shift values $\delta_i(X)$ for each conformational state X, against the measured values δ_i^*,

$$P(\delta_i^* \mid X, \sigma_{\mathrm{CS}}) = \frac{1}{\sqrt{2\pi\sigma_{\mathrm{CS}}^2}} \exp(\frac{-(\delta_i^* - \delta_i(X))^2}{2\sigma_{\mathrm{CS}}^2}), \tag{17}$$

where σ_{CS} represents the uncertainty in the chemical shift measurement. Predictions of NMR chemical shifts $\delta_i(X)$ for each conformational state X were calculated using the SHIFTX2 algorithm[47] as implemented in MDTraj,[48] using the default user-specified parameters of pH 7.0 and 298 K. The predicted chemical shifts $\delta_i(X)$ are the ensemble-averaged values of predictions of each trajectory snapshot belonging to state X. Exponential reference potentials $P_{\mathrm{ref}}(\delta_i(X))$ were used for all residues i, along with an uninformative Jeffreys prior for $P(\sigma_{\mathrm{CS}})$.

Sampling the posterior distribution with BICePs. Taking together the protection factor and chemical shift data, the full posterior function is proportional to the product a prior $P(X)$ (i.e. the predicted conformational state populations), all four likelihood functions, and priors for all nuisance parameters:

$$\begin{aligned} P(X, \lambda, \sigma_{\mathrm{PF}}, \sigma_{\mathrm{CS}}^{(\mathrm{H})}, \sigma_{\mathrm{CS}}^{(\mathrm{C}\alpha)}, \sigma_{\mathrm{CS}}^{(\mathrm{N})} \mid D) \propto P(X) \prod_i \Bigg[& \frac{P(r_i^* \mid X, \lambda, \sigma_{\mathrm{PF}})}{P_{\mathrm{ref}}(r_i(X))} \Bigg] P(\lambda) P(\sigma_{\mathrm{PF}}) \\ & \cdot \left[\frac{P(\delta_i^{*(\mathrm{H})} \mid X, \sigma_{\mathrm{CS}}^{(\mathrm{H})})}{P_{\mathrm{ref}}(\delta_i^{(\mathrm{H})}(X))} \right] P(\sigma_{\mathrm{CS}}^{(\mathrm{H})}) \\ & \cdot \left[\frac{P(\delta_i^{*(\mathrm{C}\alpha)} \mid X, \sigma_{\mathrm{CS}}^{(\mathrm{C}\alpha)})}{P_{\mathrm{ref}}(\delta_i^{(\mathrm{C}\alpha)}(X))} \right] P(\sigma_{\mathrm{CS}}^{(\mathrm{C}\alpha)}) \\ & \cdot \left[\frac{P(\delta_i^{(\mathrm{N})*} \mid X, \sigma_{\mathrm{CS}}^{(\mathrm{N})})}{P_{\mathrm{ref}}(\delta_i^{(H)}(X))} \right] P(\sigma_{\mathrm{CS}}^{(\mathrm{N})}). \end{aligned}$$

To sample this posterior probability function, 10^7 steps of Markov Chain Monte Carlo (MCMC) was performed. We employed several strategies to make this sampling efficient. First, a finite grid of possible values of $\lambda, \sigma_{\mathrm{PF}}, \sigma_{\mathrm{CS}}^{(\mathrm{H})}, \sigma_{\mathrm{CS}}^{(\mathrm{C}\alpha)}, \sigma_{\mathrm{CS}}^{(\mathrm{N})}$ were used, where the sums of squared errors (SSE) were precomputed. Proposed MCMC moves were allowed to neighboring values in the grid. Grid values for parameters with Jeffreys priors were log-scaled to enforce the prior and improve acceptance ratios.

The number of grid values for each nuisance parameter was chosen to keep the acceptance ratio around 0.5. The dimensions of the array storing SSE values for $\lambda = \beta_c, \beta_h, \beta_0, x_c, x_h, b$ was carried over from Part I. Although large ($20 \times 26 \times 50 \times 7 \times 8 \times 18 = 26.2$ million values), the array could be stored in memory.

BICePs scores quantify the conformational ensembles that best agree with experimental data.

As mentioned above, quantitative comparison between different models can be performed using the BICePs score. From the work in Part II, we have 31 models of the prior population distribution $P^{(k)}(X)$ calculated using TRAM, each at different temperatures and different restraint biases. For each of these, a BICePs calculation was performed to sample the posterior distribution $P^{(k)}(X|D)$, where D is the experimental data, and the BICePs score was computed to rank the model.

To evaluate the effects of including chemical shift data, these calculations were repeated two-fold: once using only the protection factor (PF) experimental data, and once using both the protection factor and chemical shift data (PF+CS) (Figure 10). The results show that for each simulated temperature, there is a restraint bias for which the sampled conformational ensemble achieves the best overlap with experimental restraints. In all cases, BICePs scores calculated using PF+CS data are lower than for those calculated using PF data alone. This indicates that the additional use of CS data yields models that agree better with experiment than PF data alone.

When we examine the restraint bias corresponding to the best model for each temperature (Figure 10, yellow stars), we find differences between the PF and PF+CS calculations. For the PF BICePs calculations, a majority of the best models correspond to restraint bias of 1.2 kJ, while for the PF+CS calculations, a majority correspond to a restraint bias of 0.7 kJ.

We believe this may be because a gentler restraint bias is needed to produce conformations with intact secondary structure in better agreement with measured chemical shift data.

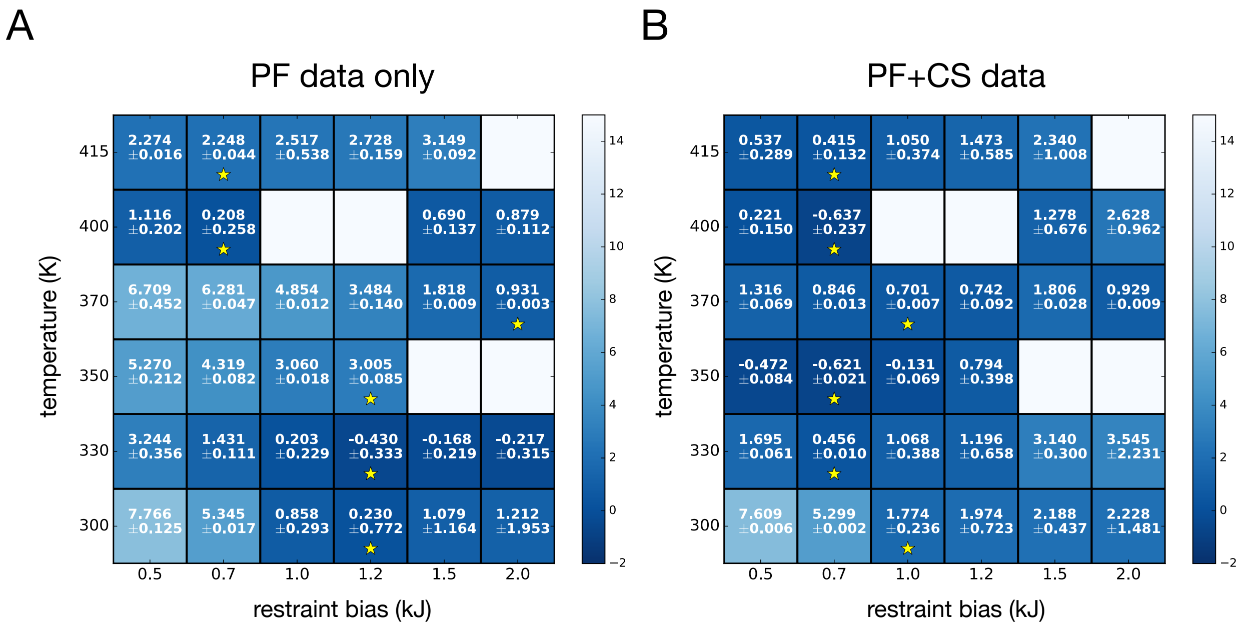

Figure 10: A summary of the BICePs scores computed for MEMMs built at different temperatures and restraint bias potentials, for BICePs calculations performed using (A) only protection factor data (PF), and (B) protection factor and chemical shift data (PF+CS). Each cell shows the computed BICePs score, with uncertainty estimates computed as standard deviations over 5 rounds of 10^7-step MCMC sampling. Blank cells indicate no models for those restraint biases were constructed due to the lack of viable trajectory input for the TRAM calculation. Cells with yellow stars mark the best model at each temperature.

A comparison of the best models at each temperature is shown in Figure 11. The model with the lowest BICePs score is one corresponding to the 400 K simulations, using a restraint bias of 0.7 kJ. For this model, we compared the populations predicted by BICePs using only the experimental data (i.e. a uniform prior $P^{(k)}(X)$) against BICePs predictions using both the experimental data and the prior given by the TRAM calculation (Figure 12). We find that, in each scenario, conformational state 18 has the dominant population. This state has an intermediate extent of structure in helix F and H, located near the middle of the tICA landscape (see Figure 8) The second-highest population, conformational state 21, has more disorder in helix F and H and is located near the right side of the tICA landscape. Using experimental restraints alone, the population of state 21 is estimated at around 15%; the prior given by the TRAM calculation, however, increases the predicted posterior population to more than 30% (Figure 12b). Other states are predicted to contribute much less population (under 1%).

The predicted state populations (Figure 12a) can be thought of as the marginal posterior distribution $P(X)$ sampled by BICePs. Marginal posterior distributions of nuisance parameters sampled by BICePs are shown in Figure 12c. For the $\sigma_{\mathrm{PF}}, \sigma_{\mathrm{CS}}^{(\mathrm{H})}, \sigma_{\mathrm{CS}}^{(\mathrm{C}\alpha)}, \sigma_{\mathrm{CS}}^{(\mathrm{N})}$ parameters, the posterior distributions give estimates of the standard errors in comparing the experimental observables against the predictions. For example, the standard error when comparing the $\ln \mathrm{PF}_i$ values against the experimental values is about two natural logarithm units. The standard error when comparing experimental versus computed chemical shifts is about 0.5, 1.1, and 2.6 ppm for H, C_α and N chemical shifts, respectively. The sampled posterior distributions for the $\sigma_{\mathrm{PF}}, \sigma_{\mathrm{CS}}^{(\mathrm{H})}, \sigma_{\mathrm{CS}}^{(\mathrm{C}\alpha)}, \sigma_{\mathrm{CS}}^{(\mathrm{N})}$ parameters are nearly identical in the two cases when only experimental restraints included (exp), and when both simulation and experimental data is included (TRAM+exp). The sampled posterior distributions for the other nuisance parameters $\lambda = (\beta_c, \beta_h, \beta_0, x_c, x_h, b)$ closely follow the posterior distributions sampled in Part I.

Using the mixture of (TRAM+exp) populations sampled by BICePs, we calculated ensemble-averaged predictions of protection factor and chemical shift observables, enabling direct comparison to the experimental values as a function of residue index (Figure 13). The results show excellent agreement with all experimental observables. The experimental and simulated N, C_α and H chemical shifts have squared correlation coefficients of $R^2 = 0.84$, 0.97 and 0.66, respectively. The good agreement is somewhat expected, as the chemical shift deviations largely report secondary structure in the structured regions of helices A, B, C, D, E and G, which is largely intact in our simulations. More remarkable is the agreement between simulated and experimental protection factors: the squared correlation coefficient for experimental and simulated values of $\ln \mathrm{PF}_i$ is $R^2 = 0.72$, which rivals Persson and Halles

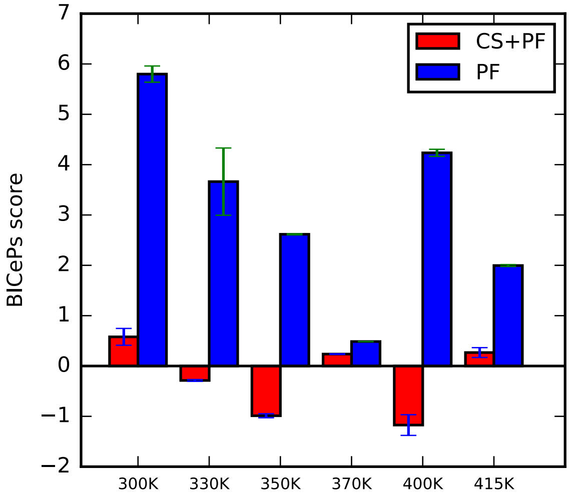

Figure 11: A comparison of the best BICePs scores at each temperature, for BICePs calculations performed with only PF restraints (blue) and PF+CS restraints (red). Error bars are standard deviations of BICePs scores computed over 5 rounds of 10^7-step MCMC sampling.

results for BPTI ($R^2 = 0.68$).[17]

Discussion

Using the methodologies described in Parts I, II and III, we have constructed a number of models of the apomyoglobin native state with different populations of conformational states, and used Bayesian inference to interrogate how well each model predicts experimental HDX protection factor and chemical shift observables. Our best model is dominated by a 70%-30% mixture of two conformational states (18 and 21), the first of which has a partially disordered yet compact helix F, and the second of which has a more disordered and solvent-exposed helix F.

Experimentally, chemical shifts are not reported for helix F residues in the apoMb N-state (pH 6.1).[30] This is because of the slow chemical exchange of these residues, presumably due to fluctuations between conformational substates. Our model, which describes multiple populations of heterogeneous conformational states, is consistent with this picture.

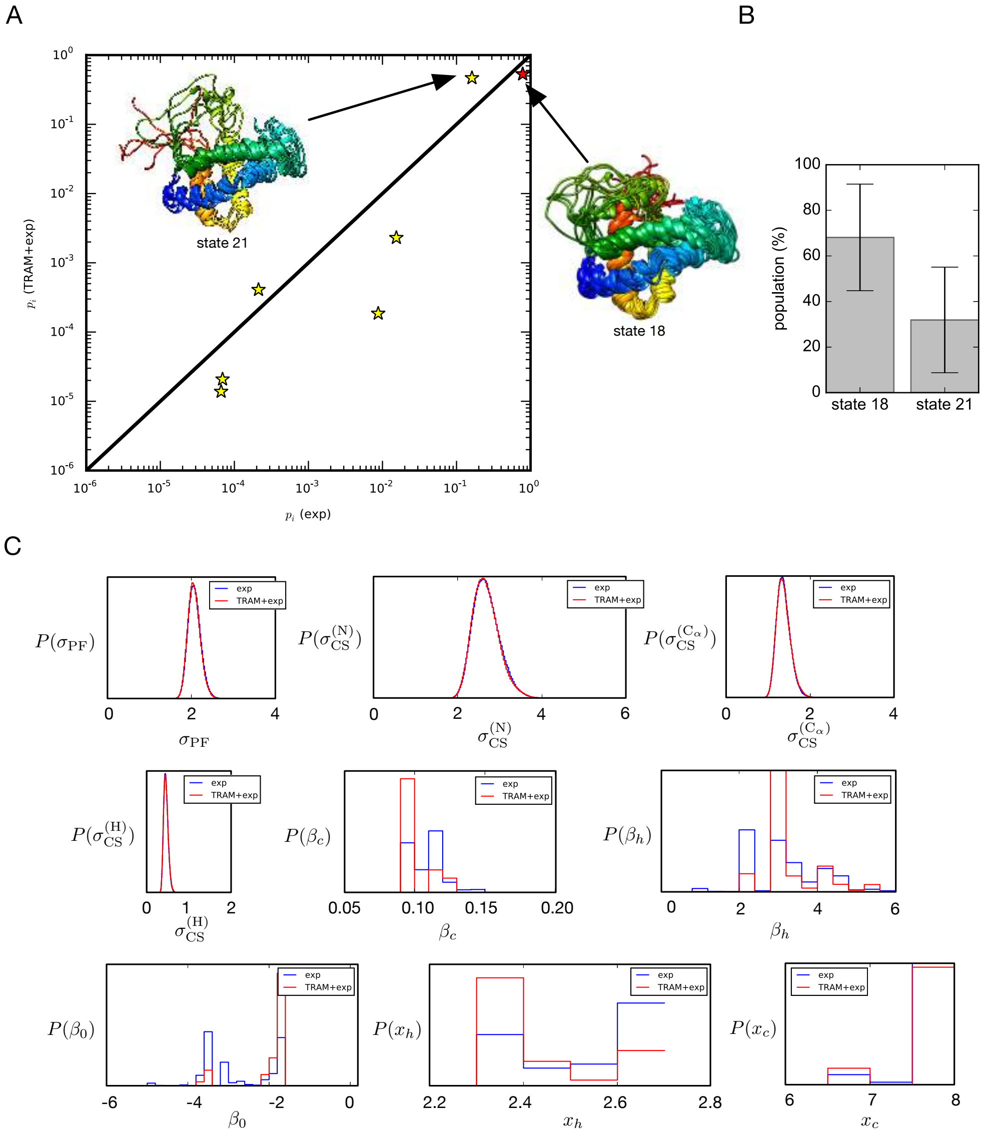

Figure 12: Posterior distributions of conformational populations and model parameters for the best-scoring model (400 K, 0.7 kJ). (A) A comparison of posterior conformational state populations p_i predicted by BICePs in the absence of simulation information (exp, i.e. a uniform prior of state populations), versus populations predicted by BICePs using both experimental information and prior conformational state populations from the best-scoring model (TRAM+exp). (B) Estimated populations of the two dominant conformational states in the model. Error bars are standard deviations of BICePs scores over 5 rounds of 10^7-step MCMC sampling. (C) Posterior distributions of all nuisance parameters sampled by BICePs, for both exp and TRAM+exp scenarios.

While here we are focused on using the TRAM method to predict equilibrium populations, this method can also be used to make predictions for the kinetics of interconversion between states. Thus, the methods developed in this work offer a way to get information about

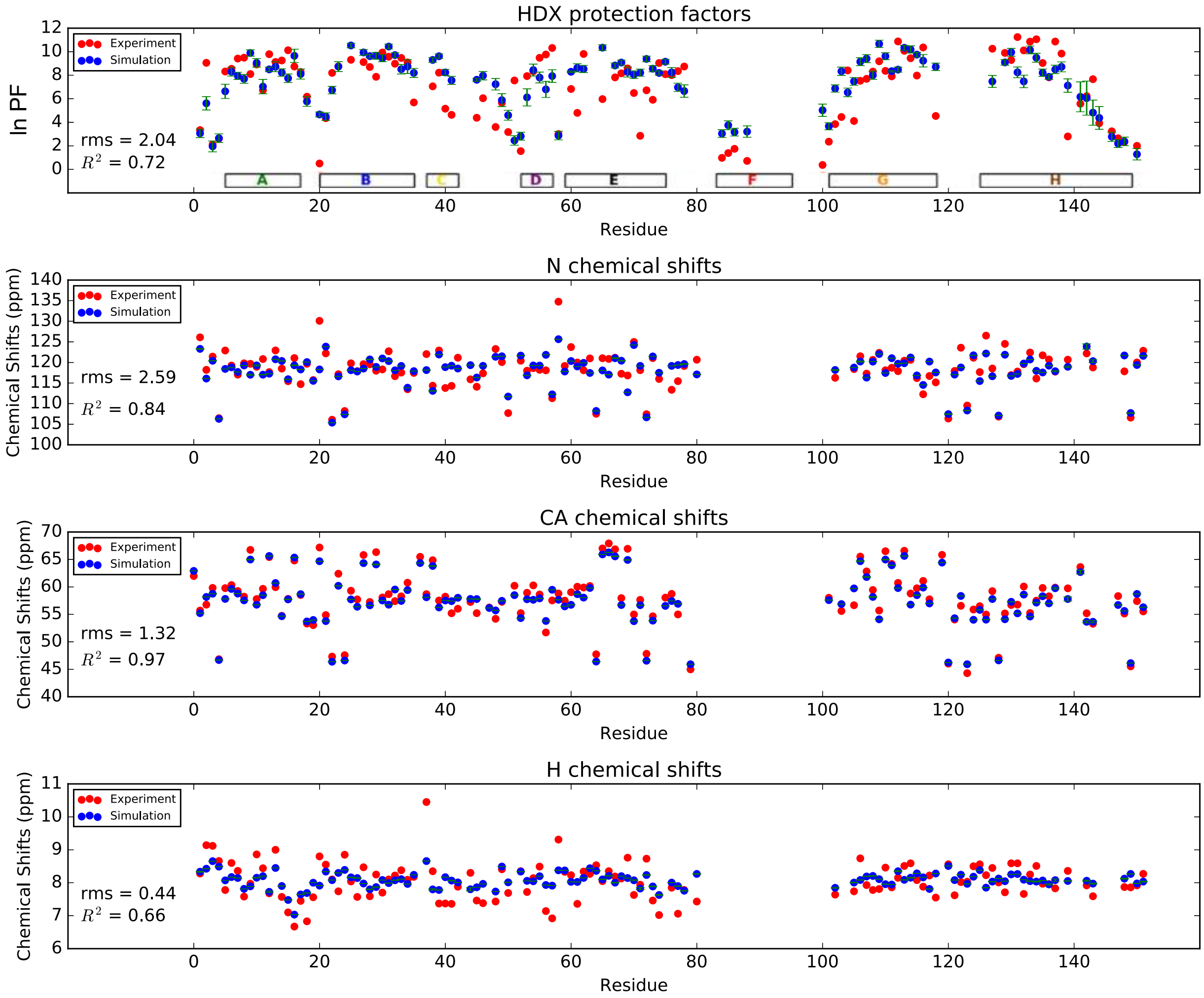

Figure 13: Residue profiles of experimental and simulated protection factor and chemical shift observables for apomylobin, using the conformational state populations of the best-scoring BICePs model (400 K, 0.7 kJ).

conformational dynamics from thermodynamically averaged experimental observables.

Another way to infer kinetic information from models of conformational state populations would be to (1) construct Markov model of dynamics in the absence of experimental information, (2) use BICePs (or some other method) to estimate improved state populations given ensemble-averaged experimental observables, and finally (3) use Maximum-Caliber method to infer changes in the transition rates between the conformational states.[49] These methods could complement and improve existing methods such as augmented Markov models[50] by providing a fully Bayesian approach to inferring model parameters.

Conclusion

In this work we have presented, in three parts, new and improved ways of reconciling simulated ensembles of protein conformations against experimental observables and applied them to modeling the N-state of apomyoglobin using HDX protection factor measurements. First, we have parameterized a new empirical predictor of HDX protection factors based on structural observables from simulation trajectory data, and applied Bayesian inference to infer the complete posterior distribution of nuisance parameters. Importantly, we show that the posterior probability gives improved results, distinct from a simple "best-fit" model.

We have also presented a new way to use bias potentials in molecular simulations to sample solvent-exposed conformations. We use this method to construct a series of multi-ensemble Markov State Models of apomyoglobin, resulting in a number of candidate models consisting of metastable conformational states and their populations.

Finally, we have used the BICePs algorithm to reconcile each model against experimental protection factor and chemical shift observables, using BICePs scores to objectively select the best model of the apomyoglobin N state. The best-scoring model is dominated by two conformational substates: one with partially disordered and compact helix F, and another with a more disordered and solvent-exposed helix F. This model agrees well with experimental protection factors ($R^2 = 0.72$), and is consistent with the observation of slow chemical exchange in the helix F region.

These tools offer new ways to refine conformational ensembles against protection factor data, utilizing the framework of Bayesian inference.

Acknowledgement

The authors thank Heinrich Roder for valuable expertise and advice, Juliette Lacomte for NMR structure refinement information for sperm whale apomyoglobin at pH 7, and D. E. Shaw Research for providing access to folding trajectory data. This work was supported by the National Science Foundation grant number MCB-140270, and in part through major research instrumentation grant number CNS-09-58854. Computing resources were supported through the Extreme Science and Engineering Discovery Environment (XSEDE) Stampede supercomputer at the Texas Advanced Computing Center (TACC).

Supporting Information Available

Supporting Tables S1, S2 and S3.

References

(1) Hvidt, A.; Linderstrom-Lang, K. *Comptes rendus des travaux du Laboratoire Carlsberg. Serie chimique* **1955**, *29*, 385–402.

(2) Bai, Y.; Sosnick, T. R.; Mayne, L.; Englander, S. W. *Science* **1995**, *269*, 192–197.

(3) Chamberlain, A. K.; Handel, T. M.; Marqusee, S. *Nature Structural & Molecular Biology* **1996**, *3*, 782–787.

(4) Arrington, C. B.; Robertson, A. D. *Methods in enzymology*; Elsevier, 2000; Vol. 323; pp 104–124.

(5) Roder, H.; Elöve, G. A.; Englander, S. W. *Nature* **1988**, *335*, 700–704.

(6) Lührs, T.; Ritter, C.; Adrian, M.; Riek-Loher, D.; Bohrmann, B.; Döbeli, H.; Schubert, D.; Riek, R. *Proceedings of the National Academy of Sciences* **2005**, *102*, 17342–17347.

(7) Englander, S. W. *Journal of The American Society for Mass Spectrometry* **2006**, *17*, 1481–1489.

(8) Petruk, A. A.; Defelipe, L. A.; Limardo, R. G. R.; Bucci, H.; Marti, M. A.; Turjanski, A. G. *Journal of chemical theory and computation* **2012**, *9*, 658–669.

(9) Ma, B.; Nussinov, R. *Journal of Biological Chemistry* **2011**, *286*, 34244–34253.

(10) Sljoka, A.; Wilson, D. *Physical biology* **2013**, *10*, 056013.

(11) Kieseritzky, G.; Morra, G.; Knapp, E.-W. *JBIC Journal of Biological Inorganic Chemistry* **2005**, *11*, 26–40.

(12) Resing, K. A.; Hoofnagle, A. N.; Ahn, N. G. *Journal of The American Society for Mass Spectrometry* **1999**, *10*, 685–702.

(13) Vendruscolo, M.; Paci, E.; Dobson, C. M.; Karplus, M. *Journal of the American Chemical Society* **2003**, *125*, 15686–15687.

(14) Best, R. B.; Vendruscolo, M. *Structure* **2006**, *14*, 97–106.

(15) Shaw, D. E.; Maragakis, P.; Lindorff-Larsen, K.; Piana, S.; Dror, R. O.; Eastwood, M. P.; Bank, J. A.; Jumper, J. M.; Salmon, J. K.; Shan, Y.; Wriggers, W. *Science (New York, N.Y.)* **2010**, *330*, 341–346.

(16) Piana, S.; Lindorff-Larsen, K.; Shaw, D. E. *Proceedings of the National Academy of Sciences of the United States of America* **2013**, *110*, 5915–5920.

(17) Persson, F.; Halle, B. *Proceedings of the National Academy of Sciences of the United States of America* **2015**, *112*, 10383–10388.

(18) Liu, T.; Pantazatos, D.; Li, S.; Hamuro, Y.; Hilser, V. J.; Woods, V. L. *Journal of The American Society for Mass Spectrometry* **2011**, *23*, 43–56.

(19) Pitera, J. W.; Chodera, J. D. *Journal of chemical theory and computation* **2012**, *8*, 3445–3451.

(20) Wu, H.; Paul, F.; Wehmeyer, C.; Noé, F. *Proceedings of the National Academy of Sciences of the United States of America* **2016**, *113*, E3221–30.

(21) Voelz, V. A.; Zhou, G. *Journal of Computational Chemistry* **2014**, *35*, 2215–2224.

(22) Ge, Y.; Voelz, V. A. *The Journal of Physical Chemistry B* **2018**, *122*, 5610–5622.

(23) Craig, P. O.; Lätzer, J.; Weinkam, P.; Hoffman, R. M. B.; Ferreiro, D. U.; Komives, E. A.; Wolynes, P. G. *Journal of the American Chemical Society* **2011**, *133*, 17463–17472.

(24) Battiste, J. L.; Li, R.; Woodward, C. *Biochemistry* **2002**, *41*, 2237–2245.

(25) Tüchsen, E.; Woodward, C. *Journal of molecular biology* **1985**, *185*, 405–419.

(26) Tüchsen, E.; Woodward, C. *Journal of Molecular Biology* **1987**, *193*, 793–802.

(27) Tüchsen, E.; Hayes, J.; Ramaprasad, S.; Copie, V.; Woodward, C. *Biochemistry* **1987**, *26*, 5163–5172.

(28) Dyson, H. J.; Wright, P. E. *Chemical Reviews* **2004**, *104*, 3607–3622.

(29) Kendrew, J. C.; Bodo, G.; Dintzis, H. M.; Parrish, R.; Wyckoff, H.; Phillips, D. C. *Nature* **1958**, *181*, 662–666.

(30) Eliezer, D.; Wright, P. E. *Journal of Molecular Biology* **1996**, *263*, 531–538.

(31) Lecomte, J. T.; Sukits, S. F.; Bhattacharya, S.; Falzone, C. J. *Protein science* **1999**, *8*, 1484–1491.

(32) Geierstanger, B.; Jamin, M.; Volkman, B. F.; Baldwin, R. L. *Biochemistry* **1998**, *37*, 4254–4265.

(33) Xu, M.; Beresneva, O.; Rosario, R.; Roder, H. *The Journal of Physical Chemistry B* **2012**, *116*, 7014–7025.

(34) Jennings, P. A.; Wright, P. E. *Science (New York, N.Y.)* **1993**, *262*, 892–896.

(35) Tsui, V.; Garcia, C.; Cavagnero, S.; Siuzdak, G.; Dyson, H. J.; Wright, P. E. *Protein Science* **1999**, *8*, 45–49.

(36) Hughson, F. M.; Wright, P. E.; Baldwin, R. L. *Science (New York, N.Y.)* **1990**, *249*, 1544–1548.

(37) Nishimura, C.; Dyson, H. J.; Wright, P. E. *Proceedings of the National Academy of Sciences* **2005**, *102*, 4765–4770.

(38) Schwantes, C. R.; Pande, V. S. *Journal of chemical theory and computation* **2013**, *9*, 2000–2009.

(39) Pérez-Hernández, G.; Paul, F.; Giorgino, T.; De Fabritiis, G.; Noé, F. *The Journal of Chemical Physics* **2013**, *139*, 015102–14.

(40) Scherer, M. K.; Trendelkamp-Schroer, B.; Paul, F.; Prez-Hernndez, G.; Hoffmann, M.; Plattner, N.; Wehmeyer, C.; Prinz, J.-H.; No, F. *Journal of Chemical Theory and Computation* **2015**, *11*, 5525–5542.

(41) Mukherjee, S.; Zhou, G.; Michel, C.; Voelz, V. A. *The Journal of Physical Chemistry B* **2015**, *119*, 15407–15417.

(42) Wakefield, A. E.; Wuest, W. M.; Voelz, V. A. *Journal of Chemical Information and Modeling* **2015**, *55*, 806–813.

(43) Rieping, W.; Habeck, M.; Nilges, M. *Science* **2005**, *309*, 303–306.

(44) MacCallum, J. L.; Perez, A.; Dill, K. A. *Proceedings of the National Academy of Sciences* **2015**, *112*, 6985–6990.

(45) Bonomi, M.; Camilloni, C.; Cavalli, A.; Vendruscolo, M. *Science Advances* **2016**, *2*, e1501177–e1501177.

(46) Shirts, M. R.; Chodera, J. D. *The Journal of Chemical Physics* **2008**, *129*, 124105.

(47) Han, B.; Liu, Y.; Ginzinger, S. W.; Wishart, D. S. *Journal of Biomolecular NMR* **2011**, *50*, 43–57.

(48) McGibbon, R. T.; Beauchamp, K. A.; Harrigan, M. P.; Klein, C.; Swails, J. M.; Hernández, C. X.; Schwantes, C. R.; Wang, L.-P.; Lane, T. J.; Pande, V. S. *Biophysical Journal* **2015**, *109*, 1528 – 1532.

(49) Wan, H.; Zhou, G.; Voelz, V. A. *Journal of Chemical Theory and Computation* **2016**, *12*, 5768–5776.

(50) Olsson, S.; Wu, H.; Paul, F.; Clementi, C.; Noé, F. *Proceedings of the National Academy of Sciences* **2017**, *114*, 8265–8270.

Supporting Information

Supporting Tables

Table S1: Experimental protection factors measured for ubiquitin taken from Craig et al.,[23] converted to ln PF values.

residue	number	ln PF
GLN	2	6.210072
ILE	3	13.7372227
PHE	4	13.4839383
VAL	5	13.1523661
LYS	6	10.6909026
THR	7	10.4629467
LEU	8	0.67005226
THR	9	0
GLY	10	3.93511792
LYS	11	5.21075007
THR	12	3.2443424
ILE	13	11.0570136
THR	14	2.53514619
LEU	15	11.5336487
GLU	16	5.14167251
VAL	17	12.2405424
GLU	18	7.97845735
SER	20	3.82459384
ASP	21	12.9796722
THR	22	7.73438333

Continued on next page

Table S1 – continued from previous page

residue	number	ln PF
ILE	23	11.2135894
GLU	24	5.00581999
ASN	25	10.5550501
VAL	26	14.6214153
LYS	27	14.8539764
ALA	28	11.4806893
LYS	29	13.4517021
ILE	30	14.2483966
GLN	31	7.7689221
ASP	32	5.6229128
LYS	33	4.56602624
GLU	34	6.21467717
GLY	35	6.26763662
ILE	36	6.981438
ASP	39	1.64174317
GLN	40	6.45875119
GLN	41	8.26167531
ARG	42	9.13435506
LEU	43	6.56927527
ILE	44	12.6573103
PHE	45	6.49328996
ALA	46	0
GLY	47	4.1699816
LYS	48	7.86102551

Continued on next page

Table S1 – continued from previous page

residue	number	ln PF
GLN	49	3.80617316
LEU	50	8.45969763
GLU	51	5.41798272
ASP	52	2.73316851
GLY	53	3.31802512
ARG	54	9.9932193
THR	55	11.3494419
LEU	56	13.0211187
SER	57	6.68440452
ASP	58	6.84098031
TYR	59	10.9580025
ASN	60	5.11404149
ILE	61	8.54949845
GLN	62	8.27088565
LYS	63	3.09927954
GLU	64	6.37125295
SER	65	7.52484808
THR	66	6.1939539
LEU	67	7.75740918
HIS	68	8.49884158
LEU	69	7.95773408
VAL	70	9.09981629
LEU	71	3.0278994
ARG	72	2.5788953

Continued on next page

Table S1 – continued from previous page

residue	number	ln PF
LEU	73	0
ARG	74	0
GLY	75	0
GLY	76	0

Table S2: Experimental protection factors measured for BPTI taken from Persson et al.,[17] converted to ln PF values.

residue	number	ln PF
CYS	5	8.52877518
LEU	6	7.43504727
GLU	7	8.229439
TYR	10	5.756463
GLY	12	3.840712
ALA	16	6.963017
ARG	17	1.752267
IIE	18	12.37639
IIE	19	2.256533
ALA	25	3.04632
GLY	28	7.676819
LEU	29	10.85899
CYS	30	3.677228
THR	32	5.701201
VAL	34	3.734793
TYR	35	11.23431

Continued on next page

Table S2 – continued from previous page

residue	number	ln PF
GLY	36	9.574149
GLY	37	11.43924
CYS	38	4.503856
LYS	41	6.988346
ARG	42	2.141404
ASN	43	5.125554
ASN	44	14.02274
SER	47	4.503856
ALA	48	2.403899
MET	52	11.02938
ARG	53	9.825131
THR	54	7.962339
CYS	55	12.1139
GLY	56	8.008391

Table S3: Experimental protection factors measured for apomyoglobin at pH 6, taken from Nishimura et al.,[37] and converted to ln PF values.

residue	number	ln PF
LEU	2	3.3387
SER	3	9.0552
GLU	4	2.1162
GLY	5	2.6101
GLU	6	8.3181
TRP	7	8.5457

Continued on next page

Table S3 – continued from previous page

residue	number	ln PF
GLN	8	9.4170
LEU	9	9.4915
VAL	10	8.0990
LEU	11	8.9169
HIS	12	6.7276
VAL	13	9.7889
TRP	14	9.1266
ALA	15	9.2542
LYS	16	10.1224
VAL	17	8.7396
GLU	18	8.2774
ALA	19	6.1741
VAL	21	0.5004
ALA	22	4.3512
GLY	23	8.1983
HIS	24	8.7599
GLN	26	9.3119
ILE	28	9.1152
LEU	29	8.6984
ILE	30	7.8670
ARG	31	9.9290
LEU	32	9.5716
PHE	33	8.9773
LYS	34	9.4717

Continued on next page

Table S3 – continued from previous page

residue	number	ln PF
SER	35	9.0890
HIS	36	5.6884
THR	39	7.0556
LEU	40	8.2188
GLU	41	5.1578
LYS	42	4.6338
PHE	46	4.3853
LYS	47	6.0469
LEU	49	3.6004
LYS	50	5.6584
THR	51	3.1733
GLU	52	7.5530
ALA	53	1.5526
GLU	54	7.9263
MET	55	8.3330
LYS	56	9.4799
ALA	57	9.7606
SER	58	10.3153
GLU	59	3.0033
LEU	61	6.8314
LYS	62	4.8015
LYS	63	9.8059
VAL	66	5.9719
VAL	68	7.8175

Continued on next page

Table S3 – continued from previous page

residue	number	ln PF
LEU	69	8.1635
THR	70	8.5773
ALA	71	6.4889
LEU	72	2.8538
GLY	73	6.7213
ALA	74	5.9142
ILE	75	9.0367
LEU	76	8.0870
LYS	77	8.0141
LYS	78	8.3490
LYS	79	8.7400
GLU	85	0.9784
LEU	86	1.3868
LYS	87	1.7472
LEU	89	0.7190
ILE	101	0.3748
LYS	102	2.3550
TYR	103	3.8462
LEU	104	4.4498
GLU	105	8.4099
PHE	106	4.1129
ILE	107	7.5292
SER	108	7.6937
GLU	109	8.3079

Continued on next page

Table S3 – continued from previous page

residue	number	ln PF
ALA	110	9.1859
ILE	111	8.3689
ILE	112	7.9042
HIS	113	10.8719
VAL	114	10.0759
LEU	115	9.4460
HIS	116	7.9725
SER	117	10.3608
HIS	119	4.5392
GLN	128	10.2523
ALA	130	9.8983
MET	131	9.2917
ASN	132	11.2423
LYS	133	10.1108
ALA	134	10.8549
LEU	135	11.0577
GLU	136	9.0395
LEU	137	7.8229
PHE	138	10.8617
ARG	139	9.8380
LYS	140	2.7987
ILE	142	5.5787
ALA	143	6.2290
ALA	144	7.6644

Continued on next page

Table S3 – continued from previous page

residue	number	ln PF
LYS	145	3.9210
LYS	147	3.2341
GLU	148	2.6429
LEU	149	2.3232
TYR	151	2.0006

Graphical TOC Entry

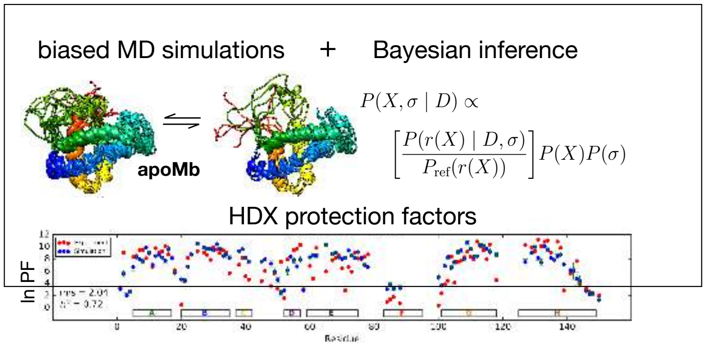
biased MD simulations + Bayesian inference
apoMb
$P(X,\sigma \mid D) \propto \left[\frac{P(r(X) \mid D,\sigma)}{P_{\mathrm{ref}}(r(X))}\right] P(X)P(\sigma)$
HDX protection factors
Experiment
Simulation
ln PF
12
10
8
6
4
2
0
rms = 2.04
R^2 = 0.72
A
B
C
D
E
F
G
H
0
20
40
60
80
100
120
140
Residue